A Simple ANN-Aided Virtual-Space-Vector PWM Strategy for Three-Level NPC Traction Inverters with Coordinate-Data Mapping

Feng Guo, *Member, IEEE*, Yuan Gao, *Member, IEEE*, Tao Yang, *Senior Member, IEEE*, Serhiy Bozhko, *Senior Member, IEEE*, Tomislav Dragičević, *Fellow, IEEE*, Patrick Wheeler, *Fellow, IEEE*, and Yue Zhao, *Senior Member, IEEE*

***Abstract*—The three-level neutral-point-clamped (3L-NPC) inverter is a mature topology that tends to be a good candidate in high-power traction applications, such as electric vehicles (EVs). However, the wide operating range under off-road scenarios inevitably renders a high modulation index and lower load angle, which affects the neutral-point (NP) voltage imbalance of the 3L-NPC inverter. To address this demerit, the prior-art virtual-space-vector pulse-width-modulation (VSVPWM) strategy has been explored due to average-zero NP currents for all ranges of load conditions. Nevertheless, this solution raises execution costs due to the complicated subsector and determination of dwell-time. To this end, in this paper, a novel artificial neural network (ANN)-aided VSVPWM is therefore proposed by leveraging the sextant-coordinate system. The designed ANN attains excellent training performance with negligible errors. More importantly, all the trained nets are designed with simple structures for running efficiently on commercial digital signal processors (DSPs). This makes the presented artificial intelligence (AI)-based modulation algorithm possible to be executed in a commercial controller of future EV powertrains. Based on the training data collected by coordinate-based derivations and the trained nets, the feasibility and effectiveness of the presented ANN-aided PWM technique were validated by simulation study through Simulink/PLECS and experimental results from a 3L-NPC traction inverter.**

***Index Terms*—Artificial neural network (ANN), coordinate-based data training, three-level topology, virtual space vector.**

I. Introduction

IN addition to the megatrends of passenger EVs to deliver people in daily life, the green transportation concept is getting huge attention from off-road automotive companies. For example, Caterpillar Inc. has announced the first battery electric 793 large mining truck. One of the innovations of heavy-duty EVs is the powertrain systems containing a high-power converter-fed high-torque traction motor, as shown in Fig. 1. Since such an electrified powertrain will haul the truck from one mining site to another, efficiency and reliability become two key aspects that should be considered carefully. Regarding high-performance traction drives, the two-level (2L) inverter is widely used in industry applications, such as grid-tied [1] and [2], more-electric aircraft [3]-[5] and electrified propulsion system [6]-[8] owing to its simplicity in prototyping and controls. Compared with the traditional 2L counterpart, the 3L-NPC converter, which is one of the most technologically mature multilevel topologies, is favorable for lower *dv/dt* and EMI emissions, filter design and reduced voltage stress.

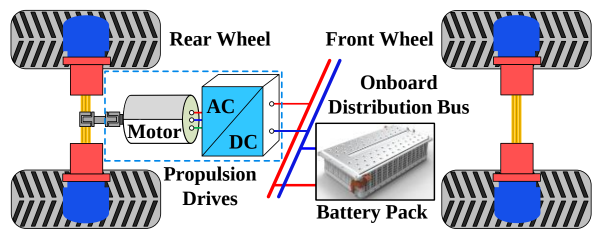

Fig. 1. The configuration of the next-generation heavy-duty EV powertrain.

However, it is noted that the normal operation of the 3L-NPC converter entails two balanced capacitor voltages. In contrast to hardware-intensive efforts, such as the front-end circuit [9], the pulse-width-modulation (PWM) strategy is a simple alternative to maintain the NP voltage in a balanced state. Authors in [10] and [11] revealed the NP drift-prone region for the traditional center-aligned seven-segment space vector modulation (SVM) strategy and identified the presence of low-frequency NP potential fluctuation. To achieve good NP voltage balance capability for all loads, the virtual-space-vector (VSV) modulation scheme was proposed in [12]. A series of VSVs is established by basic space vectors with a dedicated proportion. Several recent research attempts have been developed on the basis of this concept and have been incorporated with advanced control algorithms, such as the modulated model predictive control (M^2PC) method [13]. Nevertheless, compared with the traditional SVM method, one of the downsides of the VSV strategy is the design complexity because of subsector repartition, multi-segment pulse train generation, and dwell times determination. As a result, the implementation effort will tremendously increase when the NPC topology produces a higher output voltage level.

To relieve this crucial but complex process for the SVM, one emerging technique is to harness machine learning (ML) algorithms where the ANN is one of the most common ML models. An ANN-based PWM of a 3L inverter was proposed in [14]. However, it attempts to use ANN to map the switching sequence rather than subsector identification or duty cycle calculation. An ANN-based SVM of a five-level inverter was proposed in [15]. Though the adopted ANNs covered both sector identification and duty cycle calculation, only simulation results were presented, thus no analysis of the experimental performance is available (e.g., delay compensation, regulation, computation burden). In [16], a fast and universal neuro SVM was proposed for multilevel inverters with an arbitrary number

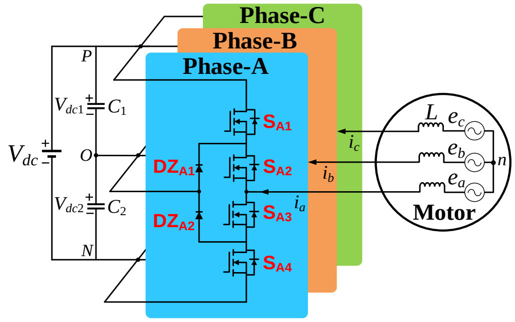

Fig. 2. The schematic of the 3L-NPC traction inverter.

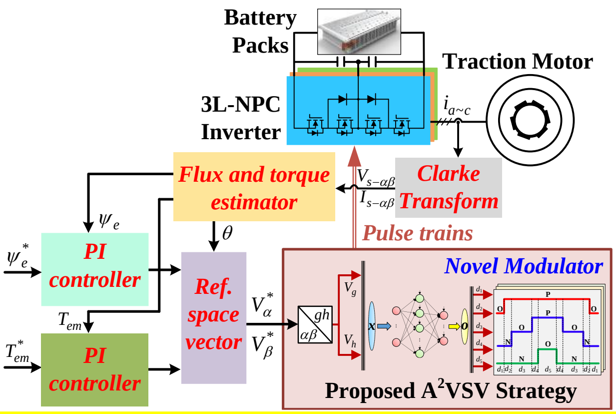

Fig. 3. Control diagram of the proposed A^{2}VSV scheme for the studied electric traction drive applications.

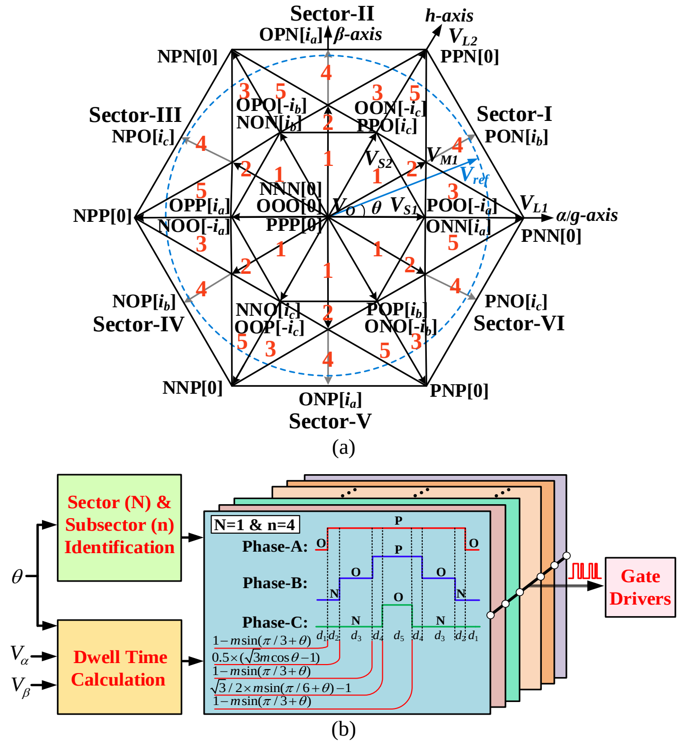

Fig. 4. (a) Space-vector diagram (SVD) of the VSVPWM strategy. (b) The conventional implementation of VSVPWM strategy.

of levels. This method is based on an ANN classifier for sector identification only, thus the duty cycle was not calculated by ANN. Besides, the works of [17] proposed a random forest (RF) regression-based SVM strategy for the induction motor drive (with a 2L inverter), where RF maps from the orthogonal α-β plane-based voltage vectors (V_α and V_β) to the duty cycles (no subsector identification). In that initiative, ANN and neuro-fuzzy inference were used as two other candidates for the same mapping. The authors found RF superior to ANN and fuzzy inference in all their experimental tests; nevertheless, the ANN-based method used a "2-40-3" structure which is so complex that it was unrealistic to implement it for the common use in industry. Following the same ANN design, i.e., mapping V_α and V_β to duty cycles, reference [18] proposed an ANN-based SVM strategy for a 2L wideband-gap (WBG)-based inverter feeding an RL load. Though the proposed solution was experimentally verified, only the computation time of real-time simulation was analyzed and the proposed ANN layer structure "2-20-3" is still quite cumbersome for real-world applications. Reference [19] also used deep reinforcement learning in this topic, but the results are from offline simulation only. [20] gives a review of artificial intelligence applications for space vector PWM-based inverters, but most of the references are before 2021, and no discussions about the industry application.

Hence, both ANN and other ML models associated with SVM have already been tried for power converters. Still, nearly all the reported methods use complex ANN structures and have only been implemented in the simulation [14], [15], [19], [21-23] or in hardware-in-loop (HIL) platforms [18]. They may not be suitable for the industrial applications due to extremely limited computation resources of microcontrollers, such as digital signal processors (DSPs), without using any host PC computation resources. As seen from [24], an overview of DSP-based implementation of ML methods for power electronics and motor drives, none of the references is using a light ANN design in the PWM strategy with DSPs.

To this end, this paper proposes a novel ANN-aided VSV (A^{2}VSV) modulation technique for 3L-NPC traction inverters, aiming to realize the proof-of-concept in heavy-duty EVs. The proposed PWM can run simple and fast VSV-based ANNs on an off-the-shelf DSP with C-language codes, thus keeping NP potential balanced in the most severe operating conditions of the studied EV powertrains. Two different data-driven modes (i.e., classification and regression) of ANN are explored for two independent parts: subsector identification and duty cycle calculation. Furthermore, the proposed A^{2}VSV technique is a model-free solution, thus it should not be constrained to the 3L-NPC topology. The introduction and preliminary results of this work have been presented in [25].

The remaining part of this paper is structured as follows. In Section II, the operating principle of the 3L-NPC drivetrain systems is introduced. In Section III, the fundamentals of ANN are briefly reviewed. Section IV investigates the ANN-based PWM concept for 3L-NPC inverters alongside simulation support. In Section V, the proposed A^{2}VSV algorithm and proprietary implementation are presented. The experimental results are provided in Section VI. The comparison of modulation performance is discussed in Section VII. Section VIII summarizes the main conclusions of this work.

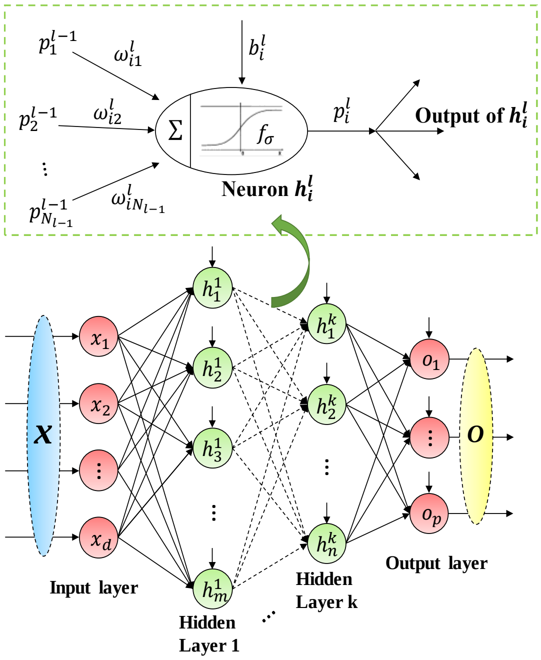

Fig. 5. Schematic of a feedforward ANN.

TABLE I
SWITCHING PRINCIPLE OF THE 3L-NPC CONVERTER

Switching State	Gating Signals S_{x1}	S_{x2}	S_{x3}	S_{x4}	Output Voltage Level
[P]	1	1	0	0	$V_{dc}/2$
[O]	0	1	1	0	0
[N]	0	0	1	1	$-V_{dc}/2$

II. Three-level NPC Electric Powertrain Systems and Operation Principles

A. Principles of Three-Level NPC Powertrain

The schematic of the 3L-NPC converter is shown on Fig. 2. Each phase comprises four switching devices (VT_{x1}~VT_{x4}) and two clamping diodes (DZ_{x1} and DZ_{x2}), where $x \in$ {A, B and C}. Two equal capacitors (C_1 and C_2) are series-connected to form the dc-link. VT_{x1} is complementarily switched with VT_{x3}. VT_{x2} and VT_{x4} follow the same manner. The switching state [P] means the gating signal (S_{x1}, S_{x2}) is (1, 1), which represents an output voltage of $V_{dc}/2$. The switching state [N] means the gating signal (S_{x1}, S_{x2}) is (0, 0), which refers to an output voltage of $-V_{dc}/2$. V_{dc} is defined as the dc-link voltage. Otherwise, the gating signal (S_{x1}, S_{x2}) is chosen as (0, 1), the output voltage is zero and the switching state is expressed as [O]. Thus, 27 SVs can be generated over a line cycle, wherein desired ones are selected to approximate the reference SV (V_{ref}), and then the dedicated pulse trains are configured at every switching cycle. Table I gives the relationship among switching state, switch status and output voltage level [26].

The overall control diagram of the investigated off-road EV is presented in Fig. 3. As can be seen, the conventional direct torque control (DTC) strategy has been applied to the PMSM, together with the introduced ANN-aided VSV modulator. The magnitude and position of the reference space vector (SV) is

TABLE II
SUBSECTOR IDENTIFICATION CRITERIA FOR SECTOR-1

Subsector	Identification Criteria
1	$0<V_g+V_h\le 0.5$
2	$V_g+V_h>0.5 \&\& V_h+2V_g\le 1 \&\& 0.5V_g+V_h\le 0.5$
3	$V_h+2V_g>1 \&\& 0.5V_g+V_h<0.5 \&\& V_h\ge 0$
4	$V_g+V_h<1 \&\& V_h+2V_g\ge 1 \&\& 0.5V_g+V_h\ge 0.5$
5	$V_g\ge 0 \&\& 0.5V_g+V_h>0.5 \&\& V_h+2V_g\le 1$

TABLE III
DWELL TIME EXPRESSIONS FOR SECTOR-I

Subsector	d_1	d_2	d_3
1	$2g$	$2h$	$1-2(g+h)$
2	$2(1-g-2h)$	$2(1-h-2g)$	$3[2(g+h)-1]$
3	$2(1-2h-g)$	$2g+h-1$	$3h$
4	$3(1-g-h)$	$2g+h-1$	$2h+g-1$
5	$2(1-2g-h)$	$2h+g-1$	$3g$

obtained as the output of traditional PI controllers for torque and flux. This indicates that the flux and torque can be controlled independently under the EV's mission profile.

B. Virtual-Space-Vector Modulation Strategy Based on the Orthogonal Coordinate System

Compared with the classic SVM strategy, the VSVPWM method introduces additional switching states and leverages their advantages. SVs are used to guarantee an average zero NP current, thus gaining NP voltage balance for all loads.

The space vector diagram (SVD) of the VSV-based solution is shown in Fig. 4(a). As shown, the hexagon is divided into 6 sectors, and each sector contains 5 subsectors that define the reference SV synthesizing region. Moreover, the subscript value of the switching state refers to the associated NP current. It can be seen that the repetition of each sextant results in complexity. Additionally, with the traditional α-β reference plane [27], massive trigonometric operation-based dwell times most likely render the designed PWM process less competitive. Fig. 4(b) elaborates on the original modulation process of the VSVPWM strategy under the orthogonal plane.

C. Sextant Coordinate System

To streamline the proposed ANN mapping process hereafter, the *g-h* reference frame is utilized. The transformation matrix is expressed in the following:

$$\begin{bmatrix} V_g \\ V_h \end{bmatrix} = \begin{bmatrix} 1 & -1/\sqrt{3} \\ 0 & 2/\sqrt{3} \end{bmatrix} \begin{bmatrix} V_\alpha \\ V_\beta \end{bmatrix} \tag{1}$$

Then, V_g and V_h can be expressed by projecting the volt-second balance rule into this new plane [3]:

$$\begin{cases} V_g = X_g d_1 + Y_g d_2 + Z_g d_3 \\ V_h = X_h d_1 + Y_h d_2 + Z_h d_3 \end{cases} \tag{2}$$

where (V_g, V_h), (X_g, X_h), (Y_g, Y_h) and (Z_g, Z_h) denote the coordinates of V_{ref} and VSVs in the *g-h* frame, respectively.

For convenience, all SVs are normalized to the magnitude of the large vector ($2V_{dc}/3$). Hence, (V_g, V_h) can be further expressed as (g, h). Tables II and III present the subsector (n) identification criteria and dwell time expressions for Sector-I.

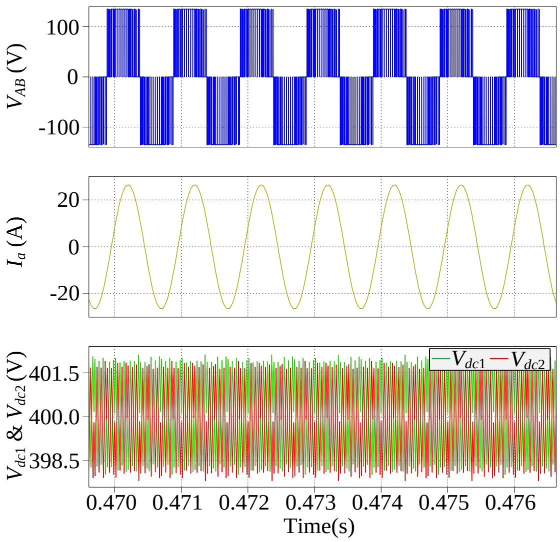

Fig. 6. Simulation results using ANN_0, MI=0.4.

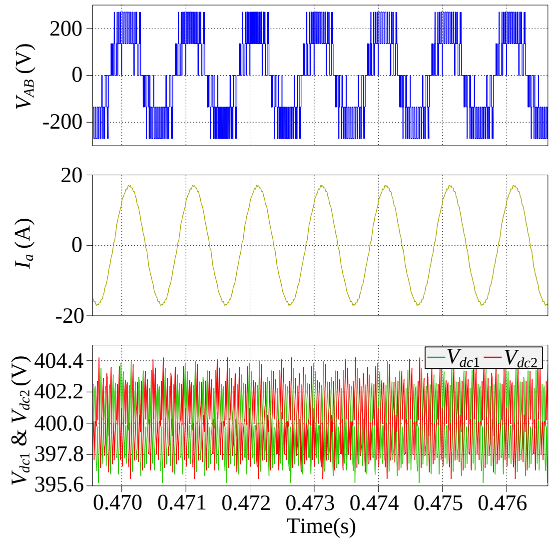

Fig. 7. Simulation results using ANN_0, MI=0.9.

III. Fundamentals of Artificial Neural Network

Fig. 5 shows the schematic diagrams of a feedforward ANN and the mathematical operation in a hidden-layer neuron h_i^l. A neuron is a mathematical function that models the functioning of a biological neuron [28] and [29]. A basic feedforward ANN comprises an input layer (x, marked in red), one or more hidden layers (h, marked in green), and an output layer (o, marked in red). The number of neurons in input/output layers is determined by the designed inputs/outputs, which usually have specific physical meanings and should vary for different topics. In contrast, the number of layers and neurons for hidden layers can be set by an algorithm developer to pursue a good mapping performance (if necessary) during the training process [30] and [31].

In Layer 1, a neuron output p_1^1 takes the form of inputs via a normalization, that is:

$$p_i^1 = N(x_i), i = 1, \ldots, N_1 \tag{3}$$

where N_1 denotes the neuron number of Layer 1.

In a hidden layer l, for a certain neuron h_i^l, the outputs of all the neurons p_i^{l-1}, in the last layer should be multiplied by the weights ω_{ij}^l and then the bias b_i^l will be added, as shown at the top of Fig. 5. After that, the result is further processed through an activation function f_σ that usually takes the form of a sigmoid function

$$f_\sigma(A) = 1/(1+e^{-A}) \tag{4}$$

to give the output p_i^l. Therefore, the operation for hidden-layer neurons can be concluded as ($l = 2, \ldots, L$-1):

$$p_i^l = f_\sigma(\textstyle\sum_{j=1}^{N_{l-1}} \omega_{ij}^l p_j^{l-1} + b_i^l), i = 1, \ldots, N_l \tag{5}$$

This output then becomes one of the inputs for the next layer (hidden or the output), l+1, and the same procedure is repeated for all the hidden-layer neurons.

Similarly, the output layer typically uses the linear activation function to integrate signals from the last hidden layer L-1 for the desired output data o_i via an anti-normalization:

$$o_i = N^{-1}(\omega_i^L p_i^L + b_i^L), i = 1, \ldots, N_L \tag{6}$$

In the next section, this paper first uses the feedforward ANN in a conventional way, which can directly generate the duty cycle by subsection and g-h coordinates but with an extensive computation burden. After that, the proposed A^2VSV is investigated to implement two kinds of mapping in the experiment: a). pattern recognition (PR) for subsection identification; b). regression for duty cycle calculation.

IV. Conventional ANN-Based Modulation Concept with Simulation Implementation

In this section, the conventional ANN method for 3L-NPC PWM is described and simulation results are presented. This method needs to use many neurons in the ANN hidden layer.

A. ANN Design in Simulation

The ANN used here is to generate the duty cycle by using subsector (n) and (g, h), marked as ANN_0. The subsection identification is still using the traditional method based on (g,h) (given in Table II), but it can get rid of the lookup table (LUT) for the duty cycle calculation. The mapping relationship of ANN_0 is yielded as:

$$(d_1, d_2, d_3) = F_o^{g,h}(n, g, h) \tag{7}$$

Since n and (g,h) are coupled in the ANN design, the training data should cover all five situations of n. Thus, the hidden-layer neuron number should be increased to learn the complex non-linear relationship (only one hidden layer is used for simplicity). According to 4827 input-output data pairs collected by coordinate-based derivations, when selecting 7 neurons, the root-mean-square deviation (RMSE) is around 2×10^{-4} for (d_1, d_2, d_3) prediction, which is acceptable. If 6 are selected, RMSE would be around 6×10^{-3}, not good enough for the modulation

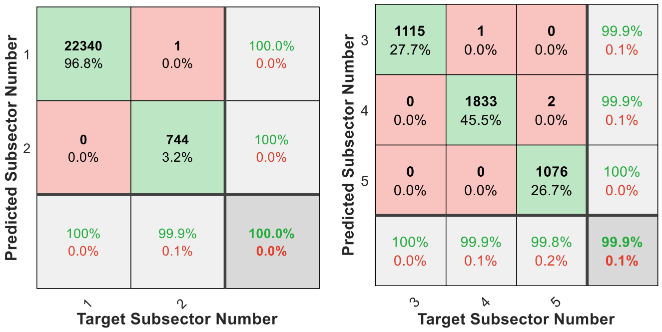

(a) (b)

Fig. 8. ANN$_1$ training performance using the confusion matrix. (a) n=1, 2 (ANN$_{1,1}$ with 1 hidden-layer neuron); (b) n=3, 4, 5 (ANN$_{1,2}$ with 2 hidden-layer neurons).

test. The trained ANN$_0$ with 7 hidden-layer neurons is then tested in the simulation.

B. Simulation Implementation

Here, the preliminary simulation study for the ANN design in Eq. (7) is conducted under a switching frequency of 16 kHz, a fundamental frequency of 50 Hz and a rated load of $6e^{j2\pi/5}\Omega$. All the parameters are summarized in Table IV.

Simulation results using the above trained ANN$_0$ are illustrated in Figs. 6 and 7, at two different modulation index (MI) conditions. In the case of MI=0.4, as shown in Fig. 6, the line-to-line voltage is characterized as three-level output. In addition, the current phase shows its sinusoidal waveform with a THD of 6.5% and two capacitor voltages are maintained in a balanced state with minimized fluctuation. In terms of a higher MI, i.e., MI=0.9, Fig. 7 displays five-level line-to-line output voltage. It should be pointed out that the load experiences a 20% reduction since the lighter load condition might be more challenging for the ANN-enabled VSV modulation technique. Furthermore, the sinusoidal phase current with a THD of 4.8% and exceptional balanced NP potential is achieved. These simulation results verify good ANN training performance and exceptional modulation performance when adopting the proposed ANN algorithm, especially for high-MI scenarios.

To implement the ANN in the adopted DSP experimentally, however, 7 hidden-layer neurons would still consume much computing power that is expected to surpass the commercial microcontroller capability. This is the primary reason why the A^{2}VSV PWM technique is proposed for experimental use, as presented in the following sections.

V. Proposed A^{2}VSV Modulation Strategy Using Sextant-Coordinate Mapping

The proposed A^{2}VSV modulation strategy is elaborated in this section for experimental use. For this approach, the n identification ANN is decoupled from the dwell-time calculation ANN. Besides, two stages are considered for the n identification. The learning modes of ML can be divided into classification and regression [32] and [33]. In the A^{2}VSV design, the n identification is based on ANN classification, while the dwell-time calculation adopts ANN regression.

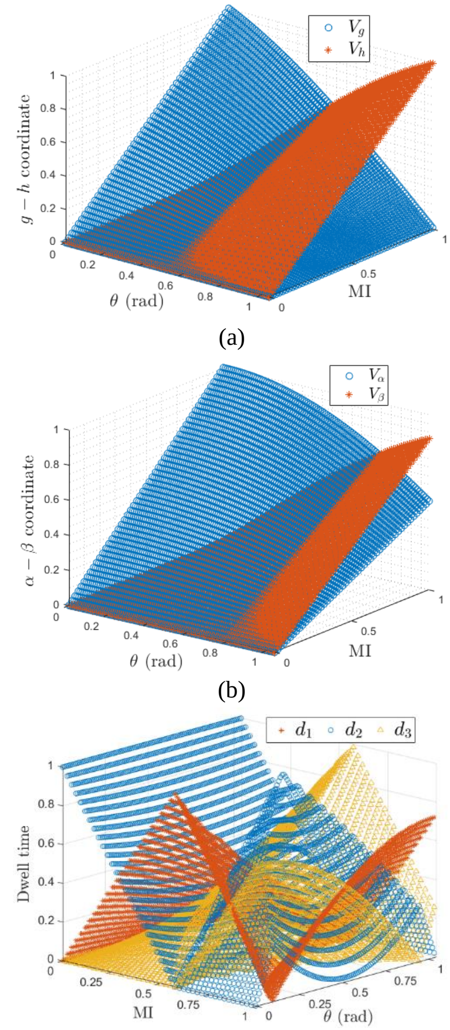

(a) (b) (c)

Fig. 9. Data generation and dwell-time calculation for ANN training based on sweeping θ and MI: (a) g-h coordinate; (b) α-β coordinate; (c) Dwell time generation.

Compared to (7), the proposed PWM method can dramatically reduce the mapping complexity.

A. ANN for Subsector (n) Identification

The first ANN part of the A^{2}VSV (ANN$_1$) is designed to map n, which has five labels/classifications. As it is to train a classifier, the ANN pattern recognition (PR) algorithm is used. Apart from the basic ANN operations in (3)-(6), PR training limits all the predictions (o_i in the output layer) into (0, 1) by the Softmax function:

$$\mu_i = e^{o_i} \Big/ \sum_{i=1}^{N_L} e^{o_i} \tag{8}$$

Each output μ_i represents the probability of "prediction is i" and the sum of all five values is 1. When given an input, the five outputs should be compared and the largest one $\mu_{i'}$ determines that the final predicted classification of this input is i'. An example of ANN PR can be found in [34], which uses ANN to imitate a predictive controller for 2L converters.

To reduce the computation burden of ANN$_1$, it is further split into two parts: $ANN_{1,1}$ for the low modulation index operating region (n=1, 2); $ANN_{1,2}$ goes for the rest subsectors (n=3, 4, 5). This is because, practically, we usually need to assume MI value and the general ranges (low or high) can be easily chosen. Two options here represent this relation:

$$(n_1, n_2) = F_{1,1}(g,h);\ (n_3, n_{4,} n_5) = F_{1,2}(g,h) \tag{9}$$

In this way, the required ANN computation capability can be significantly reduced as the output neuron number directly determines how many calculations there would be. Moreover, it becomes easier for the training of ANN_1. Fig. 8 displays the training performance with the confusion matrix of ANN_1 group. All the green numbers in this figure show the correct prediction number or percentage while the red ones are the uncorrected predictions. Each row in Fig. 8 corresponds to the performance of a predicted n class and the columns show the performance of target/raw n classes. The green cells in the diagonal of the matrix show the correctly classified number and percentage as the predicted data can match the raw data. In contrast, the other red cells show incorrect classifications. The grey cells at the right/bottom side give the normalized summation results of each row/column.

It is shown that extremely few of the subsector n predictions do not match with the sample data, which demonstrates a satisfactory training performance. This low-probability error would have a small impact on the overall modulation performance of real-time tests, see Section V.

B. ANN Mapping to Dwell Time

In this subsection, the second ANN part of A^2VSV (ANN_2) is designed to map the dwell time. Three different ANN schemes for the calculation of dwell time are proposed, which are using the g-h coordinate ($ANN_2^{g,h}$), α-β coordinate ($ANN_2^{\alpha,\beta}$) and the azimuth angle (θ)-modulation index (MI) (θ-MI) direct mapping ($ANN_2^{\theta,MI}$), respectively. All the following ANNs are trained using the same data set (4827 combinations) as the above conventional method.

1) g-h coordinate based ANN

Fig. 9(a) shows the data generation of (g, h) derived from θ and MI when V_{ref} falls into the first sector, these data sets are further used as the inputs of ANN training data. The reason for adopting the g-h coordinate is that it is simpler than target data in the orthogonal plane (α-β), and thus can be easily trained by the ANN. Since the time outputs are continuous, (3)-(6) can be directly used for mapping without a further classification/PR process. After getting the value of subsector n, the $ANN_2^{g,h}$-based duty cycle calculation can be formulated as:

$$\begin{cases} (d_{1,n}, d_{2,n}) = F_{2,n}^{g,h}(g,h) \\ d_{3,n} = 1 - d_{1,n} - d_{2,n} \end{cases} \tag{10}$$

As a result, there are five sub-ANNs in the ANN_2 group, all of which have two outputs (d_1, d_2). The reason for not including n as one of the inputs is again to save the computation burden for DSP operations. Only in this way, all the trained $ANN_2^{g,h}$ nets can utilize a 2-hidden-layer-neuron structure, which

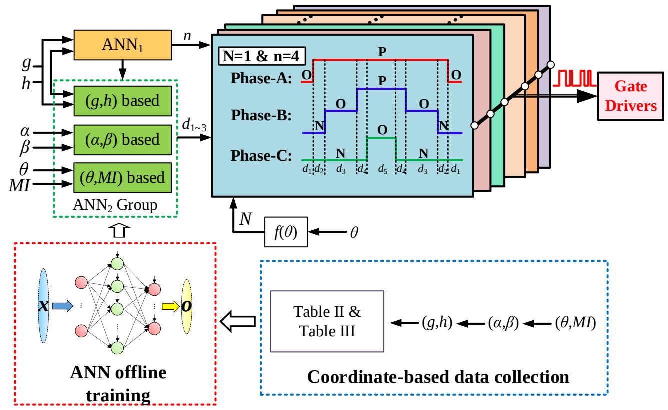

Fig. 10. Process of the proposed A^2VSV modulation scheme.

guarantees that all formulations can be easily implemented on DSPs by C-language codes.

Regarding the training performance of $ANN_2^{g,h}$, all five ANNs can predict the corresponding d_1, d_2 and d_3 with very small errors: the RMSE is less than 3×10^{-5} for every dwell-time prediction. Concerning the ANN design constraint, the linear modulation range of the modulator should also be considered. This implies that the coordinate sets for training data must be limited to avoid instability due to the null value of associated duty cycles, for example, in the first sector, data acquisition fulfills $g+h \leq 1$.

2) α-β coordinate based ANN

The second design of ANN_2 group uses the α-β coordinate, i.e., mapping from α-β to the dwell time. Fig. 9(b) shows the data generation of (α, β) derived from θ and MI. Similarly, (3)-(6) can be directly used for this mapping. After getting the value of subsector n, the α-β coordinate-based duty cycle calculation can be formulated as:

$$\begin{cases} (d_{1,n}, d_{2,n}) = F_{2,n}^{\alpha,\beta}(\alpha,\beta) \\ d_{3,n} = 1 - d_{1,n} - d_{2,n} \end{cases} \tag{11}$$

Also, for every n, all the trained $ANN_2^{\alpha,\beta}$ nets can use the 2-hidden-layer-neuron structure. The training performance of $ANN_2^{\alpha,\beta}$ is very close to that of $ANN_2^{g,h}$, all the dwell-time predictions can achieve an RMSE smaller than 3×10^{-5}. This is because the transformation between g-h and α-β is just based on a matrix which can be easily learned by ANN.

3) ANN mapping from θ-MI to dwell time

The third design of ANN_2 group leaves both g-h and α-β coordinates, directly using θ-MI as the two inputs to calculate the dwell time. Fig. 9(c) shows all the generated data results of dwell time in the whole sector (five subsectors). This design represents the following relation:

$$\begin{cases} (d_{1,n}, d_{2,n}) = F_{2,n}^{\theta,MI}(\theta, MI) \\ d_{3,n} = 1 - d_{1,n} - d_{2,n} \end{cases} \tag{12}$$

However, the training of this ANN design is much more difficult than the above two. If using the 2-hidden-layer-neuron structure, the RMSE of $d_{3,n}$ prediction would be around 5×10^{-2}.

TABLE IV
HEAVY-DUTY EV POWERTRAIN PARAMETERS

Parameters	Simulation (Section IV)	Experimentation (Section V)
Hidden-layer-neuron	7	2
Rated power	500 kVA	40 kVA
DC-bus voltage	800 V	250 V
Switching freq.	16 kHz	16 kHz
Fundamental freq.	$\leq$ 200 Hz	$\leq$ 200 Hz
Cap. (C_1=C_2)	600 µF	600 µF
Modulation index (MI)	$\leq$ 0.9	$\leq$ 0.9
Power factor (PF)	0.1~1.0	0.1~1.0

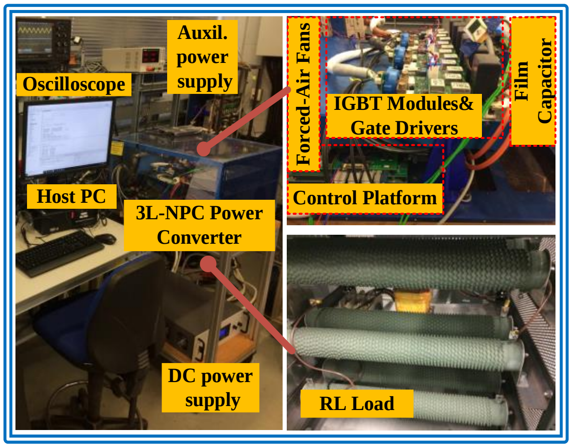

Fig. 11. Experimental test rig.

For $d_{1,n}$ and $d_{2,n}$, the RMSE is smaller but not much (around 2.7×10^{-2}). Even using 3 neurons, the $d_{3,n}$ RMSE is still around 0.01 and the RMSE of $d_{1,n}$ and $d_{2,n}$ is larger than 5×10^{-3}. The main reason for this situation is that, compared with the above two ANN design schemes, the relationship between inputs and outputs included trigonometric functions, which are not easy to be learned by the models of ANN.

In summary, training performance of $ANN_2^{g,h}$ and $ANN_2^{\alpha,\beta}$ are similar and better than that of ANN$_0$. The main reason is that the mapping complexity and training difficulties have been greatly decreased by simple and novel ANN designs. But, the training performance of $ANN_2^{\theta,MI}$ is much worse than the others. Regarding the training and test of all the above ANNs, it is using the MATLAB Deep Learning Toolbox, with Levenberg-Marquardt function. The training takes only a few seconds due to the simple design. However, the trained ANNs in MATLAB should be converted to C languages for the experimental implementation, the results will be given in Section VI.

C. Switching Pattern Determination

After the subsector identification using ANN$_1$, the output n value is utilized for selecting switching patterns which have been preset by a field-programmable gate array (FPGA) in our case. Therefore, the trained ANN$_1$ group would directly determine the switching pattern outputs. Finally, the dedicated pulse trains with dwell time are sent to gate drivers to turn on/off semiconductors accordingly. Fig. 10 summarizes the overall flowchart of the proposed A^{2}VSV PWM strategy.

From Fig. 10, it should be pointed out that Tables II and III can be updated with the inverter output level increased.

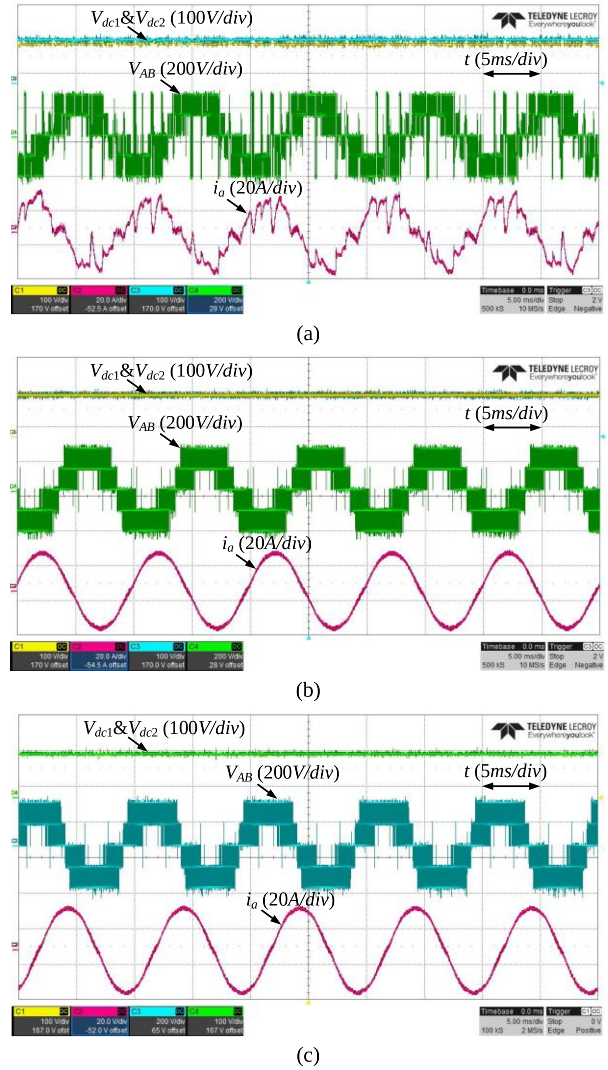

Fig. 12. The steady-state performance under MI=0.95 and PF=0.15 by the proposed A^{2}VSV strategy with (a) $ANN_2^{\theta,MI}$ (b) $ANN_2^{\alpha,\beta}$ (c) $ANN_2^{g,h}$.

Meanwhile, the model of the ANN offline training process can be inherited for VSVs in other variants of multilevel topology.

VI. Experimental Results

Before a high-power and high-torque traction motor is available to serve as the propulsive load in the studied EV powertrain systems, the modulation performance of the presented A^{2}VSV PWM strategy is experimentally verified on a scale-down IGBT-based 3L-NPC traction inverter prototype, as shown in Fig. 11. An RL load is connected to the inverter's ac side and the Delta Elektronika SM500-CP-90 bi-directional DC power supply is tied to the inverter's dc-link, miming PF angles of the assumed high-power ac machine and onboard dc-bus. The ac side parameters are monitored by a Yokogawa WT5000 precision power analyzer. The adopted control board consists of a TMS320C6713 chip and an Actel FPGA-ProAsic3 A3P400 kit. Table IV details the target drivetrain parameters.

A. Steady-State Experiments

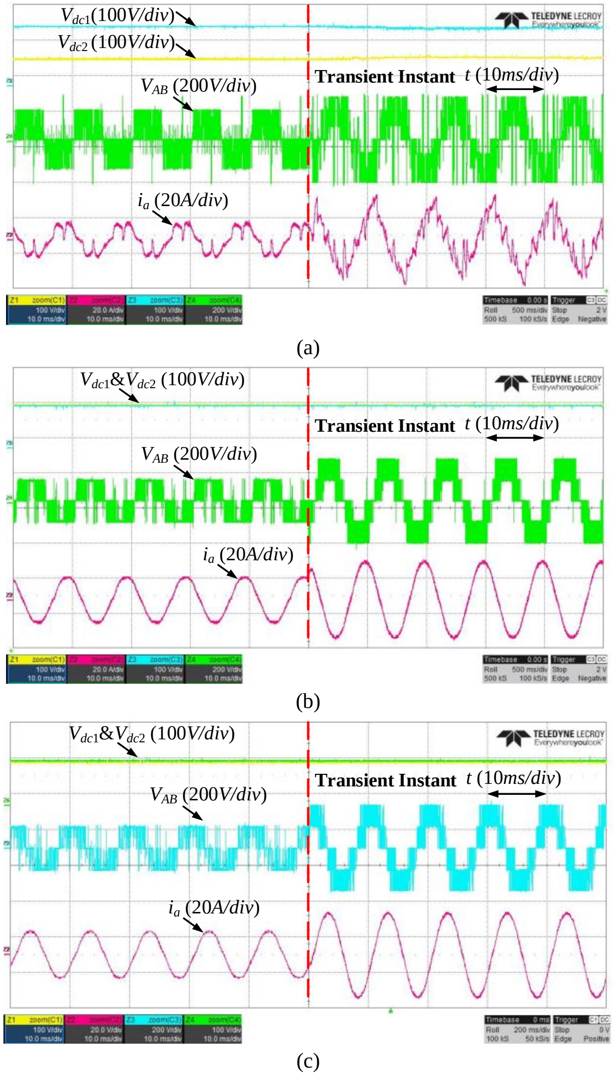

Fig. 13. The dynamic performance when MI ranges from 0.2 to 0.8 by the proposed A^{2}VSV strategy with (a) $ANN_2^{\theta,MI}$ (b) $ANN_2^{\alpha,\beta}$ (c) $ANN_2^{g,h}$.

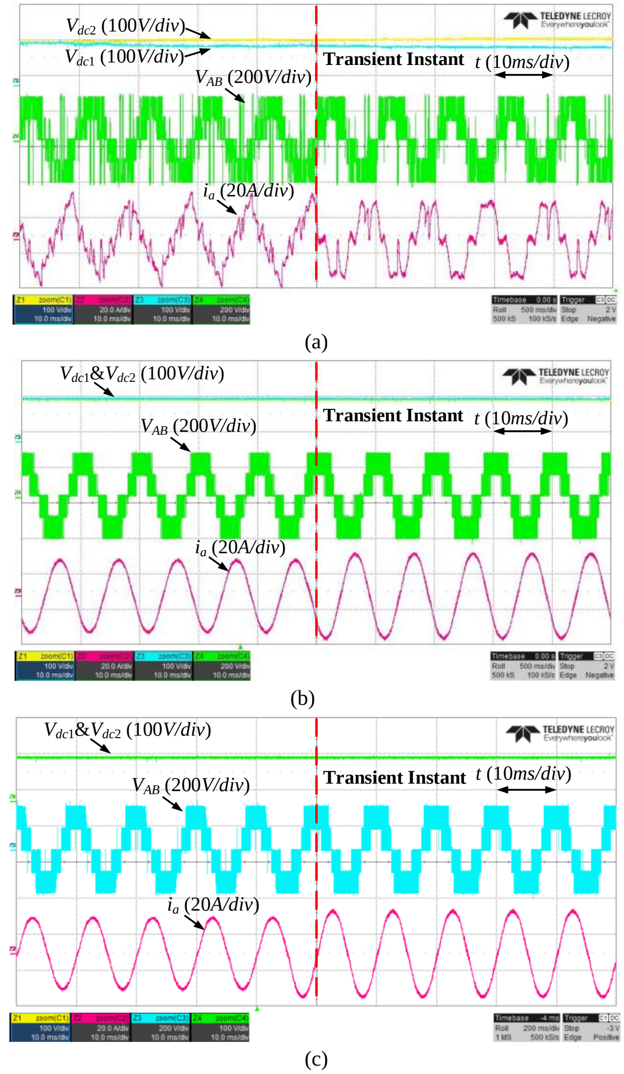

Fig. 14. The dynamic performance under the loading process by the proposed A^{2}VSV strategy with (a) $ANN_2^{\theta,MI}$ (b) $ANN_2^{\alpha,\beta}$ (c) $ANN_2^{g,h}$.

Fig. 12 shows the experimental results of line-to-line voltage, phase current and two capacitor voltages with three presented A^{2}VSV modulation strategies at an MI of 0.95 and a power factor (PF) of 0.15. It can be seen from Fig. 12(a) that, with the *θ-MI*-based ANN, line-to-line voltage and phase current are heavily distorted, and DC-link voltage fluctuation appears. In contrast to this, the *α-β* and *g-h* coordinate-based ANN are both able to ensure that two capacitor voltages are perfectly balanced, and also the five-level line-to-line voltage is characterized by overlapping areas, as shown in Figs. 12(b)-(c), which are exactly consistent with the results given in [12].

B. Transient-State Experiments

The dynamic-state performance of the proposed A^{2}VSV modulation technique is tested in the case of modulation index variation, loading process and a step-change in fundamental frequency. Fig. 13 illustrates the output variables when the modulation index ranges from 0.2 to 0.8. Different from the *θ-MI*-based ANN, where it renders deviated capacitor voltages and distorted phase voltage and current, the employed $ANN_2^{\alpha,\beta}$ and $ANN_2^{g,h}$ can realize a smooth transition ranging from low MI region to high MI region.

Fig. 14 presents the results when the active power delivered by the converter increases from 2 kW to 3 kW. It can be observed from Fig. 13(a) that the commutation error and capacitor voltage imbalance by $ANN_2^{\theta,MI}$ are severe under loading conditions, while $ANN_2^{\alpha,\beta}$ and $ANN_2^{g,h}$ perform well.

Fig. 15 displays the transient instant when the fundamental frequency is suddenly raised from 100Hz to 200Hz. Similarly, this experimentation indicates that with the help of the *α-β* and *g-h* coordinate ANN, the line-to-line voltage, phase current and NP voltage obtain good performance during the transition.

C. Distortion Analysis

The total harmonic distortion (THD) of the phase current for the proposed A^{2}VSV scheme with $ANN_2^{g,h}$ is analyzed by the FFT toolbox in MATLAB/Simulink. The resultant value is 4.86% at the modulation index of 0.2, while the THD is 3.59% at the modulation index of 0.8. In contrast, the VSV strategy based on the *g-h* reference frame is calculated as 3.42% under

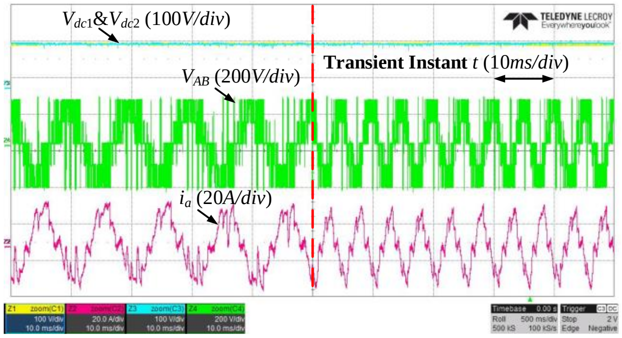

(a)

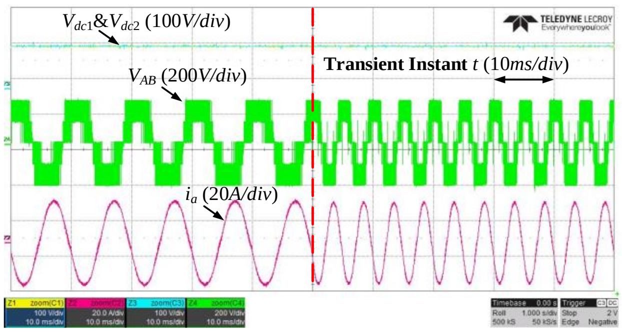

(b)

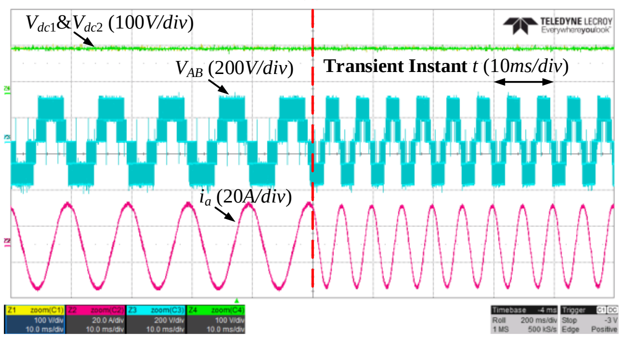

(c)

Fig. 15. The dynamic performance with a step-change in fundamental frequency with (a) $ANN_2^{\theta,MI}$ (b) $ANN_2^{\alpha,\beta}$ (c) $ANN_2^{g,h}$.

the same condition (MI=0.8). Generally, the performance is on the same level. The small THD difference of the ANN-based method is mainly due to the limited training data coverage in the operational zone; namely, the training data is limited and thus cannot precisely cover all the possible operating points. Another important reason is the training error of employed ANNs. Although $ANN_2^{g,h}$ prediction errors are very small (see Section V), the THD can be slightly affected.

Regarding the THD of $ANN_2^{\alpha,\beta}$ scheme, the distortion value is 5.32% at the MI of 0.2 and 4.80% at the MI of 0.8. Thus, it performs worse than the $ANN_2^{g,h}$ scheme even though they have similar training performance for mapping the dwell time (see Section V.B). The most tangible reason for this reason is the subsector identification (ANN_1) is using *g-h* coordinate, rather than *α-β* counterpart. As different coordinates are used in $ANN_2^{\alpha,\beta}$ scheme, the little training errors from each side could be enlarged during the online operation. For instance, if ANN_1 wrongly predicts a different subsector, the $ANN_2^{\alpha,\beta}$ prediction of dwell time can have a big error.

TABLE V
BRIEF COMPARISON WITH COMMONLY-USED SVM METHODS

Implementation Methods	Computational Burden	Distortion Control Performance	Design Complexity
g-h frame-based [3]	Less	Good	Medium
α-β frame-based [23]	Moderate-heavy	Good	High
$ANN_2^{g,h}$	Moderate	Good	Low
$ANN_2^{\alpha,\beta}$	Moderate	Good-medium	Low
$ANN_2^{\theta,MI}$	Heavy	Poor	Low

D. Computational Performance

The execution time of the proposed ANN-aided VSVPWM method is tested by the controller kit. The result shows that the *α-β* and *g-h* coordinate-based A^2VSV method cost 60.8μs and 58.3μs, in contrast to 61.5μs and 49.3μs for the original VSV scheme under *α-β* and *g-h* frame, respectively. In addition, the *θ-MI*-based ANN costs 68.2μs to implement, which consumes increased computational resources for the used DSP.

It is worth noting that the training and control performance of the *θ-MI* method can be promoted when using 3 hidden-layer neurons; however, in that case, the computational burden is enlarged, and it turns out to be infeasible for the operation on the test rig in this study.

VII. Comparison with Existing VSV Modulation Methods with Coordinate Mapping

The proposed A^2VSV strategy is compared with the *g-h* [2] and the *α-β* [23] frame-based VSVPWM strategy regarding the computational burden, robustness, and design complexity. The comparison results are detailed in Table V.

The traditional *g-h* frame-based PWM scheme features less computational burden, while the *α-β* frame-based method renders much higher computational costs. Nevertheless, this performance is moderate for the presented two ANN-based methods: $ANN_2^{g,h}$ and $ANN_2^{\alpha,\beta}$. In contrast, the $ANN_2^{\theta,MI}$ scheme turns out to have a heavy computation burden. All these methods show good robustness under different operational conditions, but only the $ANN_2^{g,h}$ scheme can achieve a very similar distortion regulation performance with the conventional methods. With the help of coordinate-mapping implementation, the design complexity is medium for the *g-h* frame-based method. The developed A^2VSV algorithm further simplifies the modulation process via the collected training data. While the *α-β* frame-based method needs to determine the subsector by using the azimuth angle of the reference SV, and then iteratively deploy dwell times of the nearest-three VSVs, which involve trigonometric functions over a fundamental period. It is worth noting that the slightly higher THD by using $ANN_2^{g,h}$ is due to conservative design in this work considering the used DSP chip. The success of this proof-of-concept will give full play to the latest strong computing power microcontrollers, thereby realizing intelligent controls and modulation for high-power density multilevel NPC topologies adopted in electrified vehicular sectors.

VIII. Conclusions

In this paper, a new ANN-aided VSVPWM strategy, with three different reference frame mapping methods, has been proposed for a 3L-NPC traction inverter. In comparison with classic implementations for PWM design, the introduced artificial intelligence (AI)-based modulator leverages ANNs to substitute complicated LUTs and derivations, thus streamlining general modulation derivation significantly. With the help of the small neuron numbers in the unique hidden layer of the introduced ANNs, achieved by C-language programming, multiple lines of *if* sentences can be dismissed by using a few simple math equations.

The key contributions of this work lie in: 1). Both subsector identification and dwell-time calculation in the conventional VSV modulation process are replaced by simple ANNs, running on DSP. 2). The trained ANNs are all designed using at most 2 hidden-layer neurons, which satisfies the light computational effort limited by the applied control platform. 3). This solution can be migrated to other enhanced VSV-based modulator variants and other NPC converters. Experimental results proved the good overall performance of the proposed strategy regarding NP voltage balance, distortion, output variables under steady and dynamic state performance, and computational effort.

Following a similar design process, the presented AI-based PWM method would chart a path to overcome the inherent design complexity arising from the SVM strategy in case switching states increase exponentially, thus generalizing to other multilevel topologies. Noteworthy, this ANN-aided modulation approach cannot correct NP voltage disturbance, nonetheless, a modified A^{2}VSV scheme with an online dwell-time-shift algorithm will be investigated in our future works.

References

[1] S. Madhusoodhanan *et al*., "Harmonic analysis and controller design of 15 kV SiC IGBT-based medium-voltage grid-connected three-phase three-level NPC converter," *IEEE Trans. Power Electron.*, vol. 32, no. 5, pp. 3355-3369, May 2017.

[2] S. Cedieu, F. B. Grigoletto, S. S. Lee, R. Barzegarkhoo and Y. P. Siwakoti, "A five-level common-ground inverter with reduced switch count for transformerless grid-tied PV applications," *IEEE Trans. on Ind. Appl.*, doi: 10.1109/TIA.2024.3412051.

[3] F. Guo, T. Yang, A. M. Diab, S. S. Yeoh, S. Bozhko, and P. Wheeler, "An enhanced virtual space vector modulation scheme of three-level NPC converters for more-electric-aircraft applications," *IEEE Trans. on Ind. Appl.*, vol. 57, no. 5, pp. 5239-5251, Sep./Oct. 2021.

[4] V. Madonna, P. Giangrande and M. Galea, "Electrical power generation in aircraft: review, challenges, and opportunities," *IEEE Trans. on Transp. Electrif*., vol. 4, no. 3, pp. 646-659, Sept. 2018.

[5] F. Guo *et al*., "An advanced dual-carrier-based multi-optimized PWM strategy of three-level neutral-point-clamped converters for more-electric-aircraft applications," *IEEE Trans. Energy Convers*., vol. 39, no. 1, pp. 356-367, Mar. 2024.

[6] D. Zhang, J. He and D. Pan, "A megawatt-scale medium-voltage high-efficiency high power density “SiC+Si” hybrid three-level ANPC inverter for aircraft hybrid-electric propulsion systems," *IEEE Trans. on Ind. Appl.*, vol. 55, no. 6, pp. 5971-5980, Nov.-Dec. 2019.

[7] F. Diao *et al*., "A megawatt-scale Si/SiC hybrid multilevel inverter for electric aircraft propulsion applications," *IEEE J. Emerg. Sel. Topics Power Electron*., vol. 11, no. 4, pp. 4095-4107, Aug. 2023.

[8] F. Guo, Z. Ma, F. Diao, Y. Zhao and P. Wheeler, "Hybrid virtual coordinate-driven CBPWM strategy of three-level T-type NPC converters for electric aircraft propulsion applications," *IEEE Trans. Ind. Electron.*, vol. 71, no. 3, pp. 2309-2319, Mar. 2024.

[9] C. Xia, X. Gu, T. Shi and Y. Yan, "Neutral-point potential balancing of three-level inverters in direct-driven wind energy conversion system," *IEEE Trans. Energy Convers*., vol. 26, no. 1, pp. 18-29, Mar. 2011.

[10] N. Celanovic and D. Boroyevich, "A comprehensive study of neutral-point voltage balancing problem in three-level neutral-point-clamped voltage source PWM inverters," *IEEE Trans. on Power Electron*., vol. 15, no. 2, pp. 242-249, Mar. 2000.

[11] J. Pou, R. Pindado, D. Boroyevich, and P. Rodriguez, "Evaluation of the low-frequency neutral-point voltage oscillations in the three-level inverter," *IEEE Trans. Ind. Electron*., vol. 52, no. 6, pp. 1582–1588, Dec. 2005.

[12] S. Busquets-Monge, J. Bordonau, D. Boroyevich and S. Somavilla, "The nearest three virtual space vector PWM - a modulation for the comprehensive neutral-point balancing in the three-level NPC inverter," *IEEE Power Electron. Lett*., vol. 2, no. 1, pp. 11-15, Mar. 2004.

[13] Y. Yang *et al*., "Low complexity finite-control-set MPC based on discrete space vector modulation for T-type three-phase three-level converters," *IEEE Trans. on Power Electron*., vol. 37, no. 1, pp. 392-403, Jan. 2022.

[14] S. K. Mondal, J. O. P. Pinto and B. K. Bose, "A neural-network-based space-vector PWM controller for a three-level voltage-fed inverter induction motor drive," *IEEE Trans. on Ind. Appl*., vol. 38, no. 3, pp. 660-669, May-June 2002.

[15] N. P. Filho, J. O. P. Pinto and B. K. Bose, "A neural-network-based space vector PWM of a five-level voltage-fed inverter," *39th IAS Annual Meeting*., 2004, pp. 2181-2187, vol. 4.

[16] M. Saeedifard, H. S. Rad, A. Bakhshai and R. Iravani, "A fast and universal neuro-based SVM algorithm for multi-level converters," *2007 IEEE Appl. Power Electron. Conf*., Mar. 2007, pp. 1508-1514.

[17] M. A. Hannan, J. A. Ali, A. Mohamed and M. N. Uddin, "A random forest regression based space vector PWM inverter controller for the induction motor drive," *IEEE Trans. on Ind. Electron*., vol. 64, no. 4, pp. 2689-2699, Apri. 2017.

[18] S. Bhattacharjee, S. Halder, A. Kundu, L. V. Iyer and N. C. Kar, "Artificial neural network based improved modulation strategy for GaN-based Inverter in EV," *2020 IEEE Canadian Conference on Electrical and Computer Engineering (CCECE)*, 2020, pp. 1-4.

[19] P. Qashqai, K. Al-Haddad and R. Zgheib, "A New Model-Free Space Vector Modulation Technique for Multilevel Inverters Based On Deep Reinforcement Learning," *IECON 2020 The 46th Annual Conference of the IEEE Industrial Electronics Society*, Singapore, 2020, pp. 2407-2411

[20] N. Zaidi, and G. Mehta. A review of application of artificial intelligence for space vector pulse width modulated inverter-based grid interfaced photovoltaic system. *International Journal of Applied*, *12*(2), 218-228, 2023.

[21] N. Langer, A. H. Bhat, and P. Agarwal, "Neural-network-based space-vector pulse-width modulation for capacitor voltage balancing of three-phase three-level improved power quality converter," *IET Power Electronics*, vol. 7, no. 4, pp. 973-983, 2014.

[22] S. A. R. Kashif, M. A. Saqib, and S. Zia, "Implementing the induction-motor drive with four-switch inverter: an application of neural networks," *Expert Systems with Applications*, vol. 38, no. 9, pp. 11137-11148, 2011.

[23] S. P. Singh *et al.*, "A 3-layered feedforward back-propagation ANN-based SVPWM control for neutral point clamped converter for PV grid integration." *Engineering Research Express*, 5.2: 025063, 2023.

[24] Al-Kaf H A G, K-B. Lee, F. Blaabjerg, "Overview of DSP-based implementation of machine learning methods for power electronics and motor drives." *Journal of Power Electronics* (2025): 1-18.

[25] F. Guo *et al*., "ANN-aided virtual-space-vector PWM strategy for three-level NPC inverter using sextant-coordinate mapping for heavy-duty EV applications," *2024 IEEE Transportation Electrification Conference and Expo (ITEC)*, Chicago, IL, USA, 2024, pp. 1-4.

[26] F. Guo *et al*., "Hybrid active modulation strategy for three-level neutral-point-clamped converters in high-speed aerospace drives," *IEEE Trans. Ind. Electron.*, vol. 70, no. 4, pp. 3449-3460, Apri. 2023.

[27] A. Choudhury, P. Pillay, and S. S. Williamson, "DC-bus voltage balancing algorithm for three-level neutral-point-clamped (NPC) traction inverter drive with modified virtual space vector," *IEEE Trans. on Ind. Appl*., vol. 52, no. 5, pp. 3958-3967, 2016.

[28] T. Guillod, P. Papamanolis, and J. W. Kolar, "Artificial neural network (ANN) based fast and accurate inductor modeling and design," *IEEE Open J. Power Electron*., vol. 1, pp. 284-299, 2020.

[29] S. Zhao, F. Blaabjerg, and H. Wang, "An overview of artificial intelligence applications for power electronics," *IEEE Trans. Power Electron*., vol. 36, no. 4, pp. 4633-4658, 2020.

[30] Z. Li, Y. Gao, X. Zhang, B. Wang, and H. Ma, "A model-data-hybrid-driven diagnosis method for open-switch faults in power converters," *IEEE Trans. Power Electron*., vol. 36, no. 5, pp. 4965-4970, 2020.

[31] S. Vazquez *et al*., "An artificial intelligence approach for real-time tuning of weighting factors in FCS-MPC for power converters," *IEEE Trans. Ind. Electron*., vol. 69, no. 12, pp. 11987-11998, 2021.

[32] Y. Gao, T. Yang, S. Bozhko, P. Wheeler, and T. Dragičević, "Filter design and optimization of electromechanical actuation systems using search and surrogate algorithms for more-electric aircraft applications," *IEEE Trans. on Transp. Electrif*., vol. 6, no. 4, pp. 1434-1447, 2020.

[33] S. Wang, T. Dragicevic, Y. Gao, and R. Teodorescu, "Neural network based model predictive controllers for modular multilevel converters," *IEEE Trans. Energy Convers*., vol. 36, no. 2, pp. 1562-1571, 2020.

[34] M. Novak and T. Dragicevic, "Supervised imitation learning of finite-set model predictive control systems for power electronics," *IEEE Trans. Ind. Electron*., vol. 68, no. 2, pp. 1717-1723, 2020.